

## MIT Open Access Articles

*New approach to 3D electrostatic  
calculations for micro-pattern detectors*

The MIT Faculty has made this article openly available. **Please share** how this access benefits you. Your story matters.

**Citation:** Lazić, P, D Dujmić, J A Formaggio, H Abraham, and H Štefancić. New Approach to 3D Electrostatic Calculations for Micro-pattern Detectors. *Journal of Instrumentation* 6, no. 12 (December 1, 2011): P12003-P12003.

**As Published:** <http://dx.doi.org/10.1088/1748-0221/6/12/p12003>

**Publisher:** Institute of Physics Publishing

**Persistent URL:** <http://hdl.handle.net/1721.1/79403>

**Version:** Author's final manuscript: final author's manuscript post peer review, without publisher's formatting or copy editing

**Terms of use:** Creative Commons Attribution-Noncommercial-Share Alike 3.0



# New approach to 3D electrostatic calculations for micro-pattern detectors

---

**Predrag Lazić<sup>a\*</sup>, Denis Dujmić<sup>b</sup>, Joseph A. Formaggio<sup>b</sup>, Hrvoje Abraham<sup>c</sup> and Hrvoje Štefančić<sup>d†</sup>**

<sup>a</sup>*Department of Materials Science and Engineering,  
Massachusetts Institute of Technology, Cambridge, Massachusetts 02139, USA*

<sup>b</sup>*Laboratory for Nuclear Science,  
Massachusetts Institute of Technology, Cambridge, Massachusetts 02139, USA*

<sup>c</sup>*Artes Calculi,  
Fra Grge Martića 24, Zagreb, Croatia*

<sup>d</sup>*Theoretical Physics Division,  
Rudjer Bošković Institute, POB 180, HR-10002 Zagreb, Croatia  
E-mail: plazic@mit.edu*

**ABSTRACT:** We demonstrate nearly approximation-free electrostatic calculations of micromesh detectors that can be extended to any other type of micropattern detectors. Using a newly developed Boundary Element Method called Robin Hood Method, we can easily handle objects with huge number of boundary elements (hundreds of thousands) without any compromise in numerical accuracy. In this paper we show how such calculations can be applied to Micromegas detectors by comparing electron transparencies and gains for four different types of meshes. We also demonstrate the inclusion of dielectric material by calculating the electric field around different types of dielectric spacers.

**KEYWORDS:** Gaseous detectors; Detector modelling and simulations II (electric fields, charge transport, multiplication and induction, pulse formation, electron emission, etc.); Micropattern gaseous detectors (MSGC, GEM, THGEM, RETHGEM, MHSP, MICROPIC, MICROMEGAS, InGrid, etc.).

---

\*Corresponding author.

†The work of Hrvoje Štefančić on this paper was performed outside his working hours at Rudjer Bošković Institute and outside facilities of Rudjer Bošković Institute.

---

## Contents

<b>1. Introduction</b>	<b>1</b>
<b>2. Theory and methods</b>	<b>2</b>
2.1 Electrostatics and Boundary Element Methods	2
<b>3. Computations and results</b>	<b>3</b>
3.1 Transparency and gain	3
3.2 Effect of dielectric spacer	5
<b>4. Conclusions</b>	<b>6</b>

---

## 1. Introduction

It has been more than two decades since micro-pattern detectors have emerged in the market. These gaseous detectors are characterized by a small distance between electrodes in the charge amplification region (tens to hundreds of  $\mu\text{m}$ ) [1]. Nowadays, these so called micro-pattern detectors (in most widely used versions as Micromegas [2] and GEMs [3]) are established as good substitutes for the multiwire proportional chamber due to their finer granularity, ability to operate at high ionization rates and simple manufacturing. Their use ranges from trackers in accelerator-based experiments, large time-projection chambers in rare-event detectors to radiation detectors [4]. Despite the widespread acceptance of micro-pattern detectors, a precise calculation of the electric field inside the three-dimensional structure of electrodes is still a challenge. In this paper we choose a Micromegas geometry as a proxy for all micro-pattern detectors, and perform three dimensional electric field calculations. We compare different mesh geometries and expected performances.

A micromesh in Micromegas detectors [2] separates the low-field conversion volume from the high-field amplification region (see figure 1). The electric field in this transitional volume depends on the geometric shape of the micromesh and affects the performance of the detector. Calculation of the electric field is difficult due to the three-dimensional nature of the problem and the high variation of the field in the small volume around the mesh. This requires a fine spatial fragmentation and leads to computational complexity that presents a problem for popular algorithms. A standard remedy is to simplify the detector geometry, e.g. by ignoring the third dimension [5] or approximating the mesh geometry [6]. We present a calculation without such compromises that uses a novel BEM algorithm [7, 8]. We calculate electronic transparency and gain for four mesh types and vary the pitch of the mesh and ratios of the drift and amplification field. Also we explore the influence of the dielectric spacer on the electric field in the device [9].

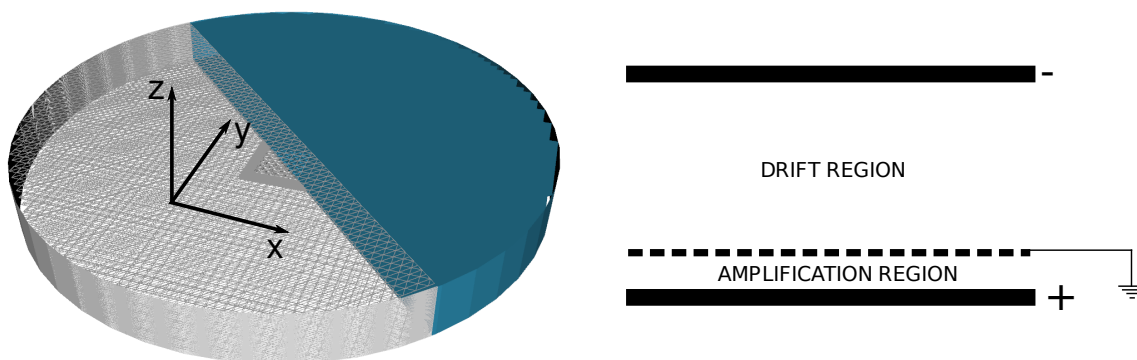


**Figure 1.** The whole detector as calculated - left. Schematic picture of the detector - right. A charged particle ionizes gas in the drift region leaving a trail of primary ionization electrons. In order to read them out, the electrons drift in a weak field through a micromesh, and enter the high-field amplification region where they undergo avalanche multiplication.

## 2. Theory and methods

To calculate the properties of the Micromegas detectors an electrostatic solution to the applied voltages is required. Having the electrostatic solution, one can simulate electron trajectories inside the detector in order to determine parameters such as transparency and gain. The interior of the detector is usually filled with some inert gas.

### 2.1 Electrostatics and Boundary Element Methods

Since the most important quantity in studying the operation of Micromegas detector is the electric field, our method of choice for electrostatic part of the problem is the Boundary Element Method (BEM) [7, 8, 11]. BEM in electrostatics consists of finding the charge density distribution on a set of given boundary elements (usually triangles) that satisfy the given boundary conditions - i.e. potential values at the surface of the electrodes. Once the charge densities are found owing to the Green's function for the Coulomb interaction, we can reconstruct the potential and electric field accurately anywhere in space. Most of the existing electrostatic codes are based on a finite differences or finite element methods [12, 13] which find potential values on a grid of points in volume respecting the given boundary conditions on electrodes. Putting aside the fact that such solutions are not solutions to Maxwell's equations [14], there is another problem in that the grid of points needs to be terminated artificially [15], introducing an arbitrary parameter into the calculations. Moreover, an impractically fine density of grid points is required in order to achieve accurate values of the electric field around corners and edges of electrodes. Such inaccuracies in the electric field values accumulate along the simulated trajectory of the particle. In contrast to finite element and finite difference methods, the biggest problem in classical BEM is the size of the Coulomb interaction matrix. This matrix is not sparse (on the contrary - it is full) and scales as  $N^2$  in memory requirements with the number of boundary elements. This limits the calculation to a mere few thousands of boundary elements [11, 15, 17], which restricts the complexity of problems and hinders the wider usage of BEM in electrostatics. In this work, we use a novel algorithm

named Robin Hood (RH) [16] which elegantly overcomes this challenge of matrix size without a compromise in accuracy. This enables us to treat systems of several hundred thousands of triangles on a single CPU. The RH code does not include a simulation of electron propagation itself. One option would be to use the *Garfield* code [5] and supply the electric field map calculated by the RH method. However, we have decided to make our own implementation of the transparency and gain calculation in order to have greater control over the output of the simulation.

### 3. Computations and results

The four types of micro-meshes that we use in our calculations, namely rectangular, cylindrical, woven and calendered are shown in figure 2.

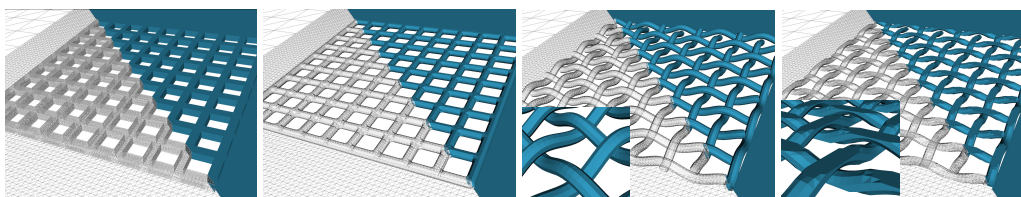


**Figure 2.** Different types of micro-mesh, from left to right: rectangular, cylindrical, woven and calendered.

We have chosen 8 different amplification-to-drift field ratios and 8 different mesh pitches while keeping in all cases the diameter/width of the wire constant at 28.2 microns. In our model, the micro-mesh detector is always positioned so that its center is at 50 microns above the bottom electrode (anode) and all voltages are fixed except the voltage of the anode. By varying the anode voltage, we achieve different drift-to-amplification field ratios. The total size of the mesh area is  $2.5\text{mm} \times 2.5\text{mm}$  – much larger than the scale of the signal spread due to e.g. electron diffusion. The number of triangles for the different types of meshes or pitches varies but is always greater than 300,000. The equipotentiality of the electrodes is satisfied to 1 part in  $10^4$ .

In the first subsection, we calculate the transparency and the gain, while in the second subsection we look at the influence of a dielectric spacer placed between the mesh and the anode. We use three different types of spacers - a horizontal filled cylinder, a horizontal hollow cylinder (capillary), and a vertical hollow cylinder - in order to study the influence of these dielectrics on the electric field inside the detector.

#### 3.1 Transparency and gain

The transparency and gain are calculated using trajectories of primary-ionization electrons that are randomly created in the drift region. The transparency is defined as the fraction of primary-ionization electrons that reach the amplification region. In order to calculate electron trajectories we use two methods. In the electric-field tracking (EFT) method, we ignore the electron diffusion in gas, and place electron trajectories along the lines of the electric field flux [6]. The electric field is calculated using charges on the electrodes. In the electron micro-tracking (MT) method [6], the ionization, electron attachment and diffusion are taken into account using tabulated values for a gas mixture ( $\text{CO}_2$  (15%), Ar (85%) at 760 Torr of pressure) [10]. In both tracking approaches,

we calculate the gain as the integral of ionization and attachment coefficients along the electron trajectory. For each calculation we sample 400 trajectories. Plots of trajectories for EFT and MT calculations are shown in figure 3.

The complete results for the electrical transparency depending on the optical transparency and amplification to drift field ratio for all four types of meshes and for EFT and MT calculations are given in figure 4. In all cases, a more realistic MT calculation yields a smaller transparency than the EFT. In the case of gain, the situation is reversed, MT calculation yields systematically smaller gain than EFT. Among the different types of meshes, cylindrical and calendered are the most transparent ones, while rectangular meshes are the least transparent.

In order to relate our calculations to experimental values, we have compared our calculation for transparency of the mesh to the results from the reference [6]. The calculated results from the reference [6] and our results for the same mesh geometry are given in figure 5. Agreement between the two calculations is excellent and considering the comparison to the experiment in the reference [6] we conclude that our calculation is in good agreement with experiment as well. Notice that the error introduced in the transparency calculation is mostly coming from the statistical procedure (Monte Carlo) of calculating transparency, it does not say anything about quality of the electrostatic solution alone.

At a fixed amplification ratio the electrical transparency grows with the optical transparency, as shown in figure 6. This is expected, but it is worth noting that for this particular set of parameters (50% optical transparency) the electrical transparency is 100%.

In the case of a fixed mesh parameter (optical transparency of 40%), the electrical transparency increases with the amplification to drift field ratio. In the MT calculations, the cylindrical, woven and calendered mesh are very similar to one another while rectangular mesh yields much lower transparencies (see figure 7). Our explanation of this differences in transparencies lies in the shape of the deflection electric field (i.e. electric field in the x-y direction), parallel to the mesh. This field deflects electrons from hitting the mesh and guides them into the holes yielding the funnel effect shown in figure 3. Electric field values in the x-y plane cross section (shown in figure 14) are given in figure 15 for all 4 types of meshes. The cause of the weakest funneling power of the rectangular mesh lies in its high symmetry which causes a large electric field cancellation in the x-y direction. This effect is to some extent present in the cylindrical mesh while in the calendered and woven mesh, the reduction in symmetry alters the shape of the  $E_{xy}$  electric field.

Explanation for the increase in the electrical transparency with increase of amplification field, as shown in figures 4,7 (i.e. increase of amplification to drift field ratio, but in our case drift field is kept constant) is as follows. Increasing the amplification field is achieved by increasing the value of the attractive potential of the anode. This is reflected in the field strength and shape around the mesh and in particular in the holes of the mesh through which the anode is "visible" to the electrons above the mesh. The metallic wires screen the field from the anode except in the holes of the mesh. In this way the holes in the mesh became much stronger attractors for electrons which following this path avoid hitting the mesh and so the electrical transparency of the mesh is increased as the amplification field is increased.

The result for the gain dependence on field ratio, given in figure 8, is interesting because it shows the four mesh geometries are practically indistinguishable in this respect. The explanation for this is rather simple. The gain is obtained as an integral of the Townsend coefficient along the trajectory of the particle as it travels from the drift region into the amplification region. All four meshes (or virtually any other shape of the mesh) generate a homogeneous field above and below the mesh in the bulk of the volume, and differences in the electric field are visible only very close to the wires. Electrons that pass near the wires account for a very small fraction of all trajectories, and therefore the mesh type has no significant influence on the gain. Hence the crucial role of the geometry of the mesh is whether the electron makes it from the drift into amplification region without colliding into the mesh and is obviously very sensitive to the details around the mesh. On the other hand, the electrons that go through achieve the gain that is almost completely determined just by the ratio of the amplification and drift field and is not sensitive to the detailed geometry.

From figure 8 we can conclude that at given field ratio gain is increased by reducing optical transparency of the mesh. In order to better understand this correlation, we performed calculations at a fixed amplification to drift field ratio varying the transparency of the mesh.

The results for the gain dependence on the transparency of the mesh at fixed amplification to drift field ratio are given in figure 9. The trend of increasing gain by reducing the transparency of the mesh can be explained by creating more homogeneous electric field regions owing to the fact that less transparent mesh resembles more a full metal electrode yielding homogeneous field in the space. However, since we are calculating the average gain - i.e. only for the trajectories that actually reach the bottom electrode, reducing the mesh transparency yields zero gain simply because none of the trajectories gets through the mesh for smaller optical transparencies. So we can notice an interesting peak in the gain at around 30% optical transparency giving the best tradeoff between this two effects - more homogeneous and stronger field and smaller transparency.

To summarize on the transparency and the gain calculations, we discuss the fact that MT calculations, which are more realistic compared to EFT, yield smaller transparencies but larger gains than EFT calculations. Explanation for this is that in the MT calculations – because of the diffusion character of the movement along trajectory (see figure 3) – the particle travels longer distance from the starting point to the bottom electrode.

### 3.2 Effect of dielectric spacer

In the practical realization of the micromesh detectors, a set of dielectric spacers is required to keep a constant gap between the mesh and the anode. The spacer is typically a dielectric cylinder, though in some cases it can have a capillary shape (hollow cylinder). We have studied two types of horizontal spacers made of fused silica which each have a dielectric constant of  $\epsilon_r = 3.5$ . The geometry of the capillary spacer is shown in figure 11. The RH code can handle dielectric materials as well as conductors. After finding the charge densities on the metal surfaces and polarizations on the dielectric surfaces (RH can handle only homogeneous dielectrics), we calculate potential and electric field values in any point in space. The cross section of the potential and electric field values along the plane from figure 10 are given in figure 12. Results for the electric field when the spacer is present are not surprising. Introducing a full dielectric cylinder causes larger perturbation in the field resulting in the increased field values in the regions where cylinder touches the electrodes

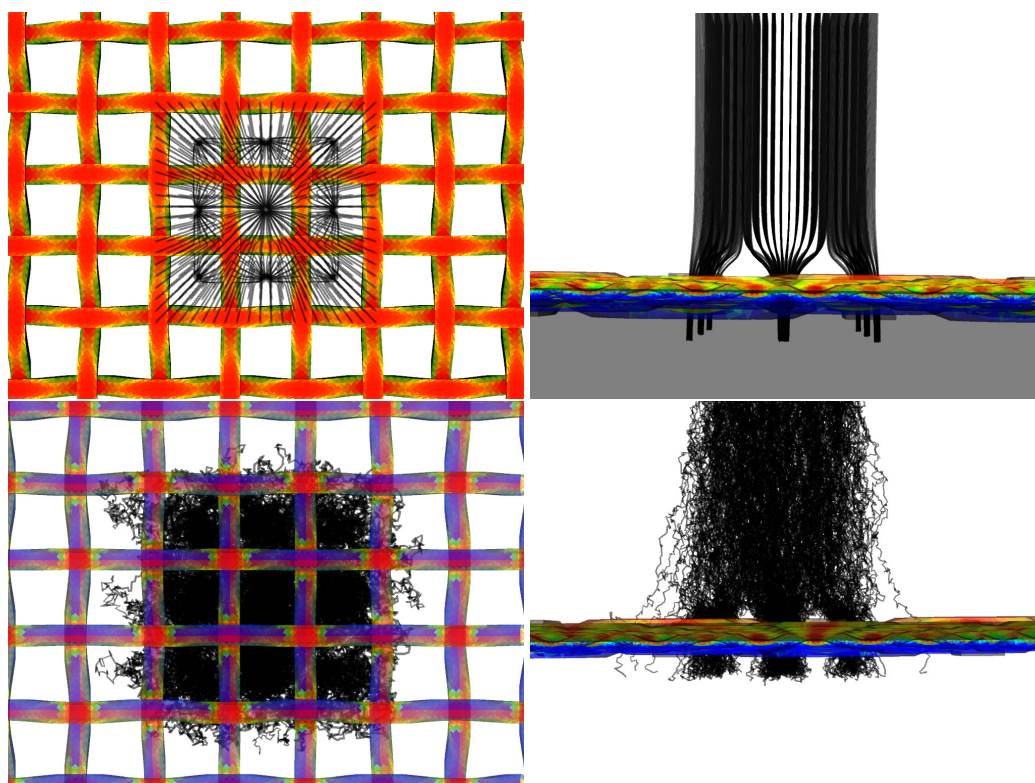


**Figure 3.** Plots of electron trajectories that follow electric field lines are shown in the two images on the top. Plots of microscopic electron tracking that take into account the electron diffusion are shown in the bottom.

(anode and the mesh). Introducing the homogeneous dielectric into the region where the electric field is present results in the reduction of the electric field value in the interior of the dielectric object [18]. This can be explained by the polarization charges at the surface of the dielectric. The larger the volume in which electric field is reduced, the larger is the surface polarization on the dielectric. On the other hand, the surface polarization on the dielectric causes an increase in the electric field close to the surface outside the dielectric. This is the reason why the electric field is more increased in the case of the full cylinder than in the case of the capillary spacer. A capillary spacer reduces the electric field produced by the surrounding electrodes only in its interior which has a much smaller volume than in the case of the full cylinder spacer. Increase in the electric field values is not welcome in the detector design since it can lead to electric discharges. Therefore the dielectric material should occupy the smallest possible volume while retaining its mechanical properties of separating the mesh from the anode.

We obtain qualitatively the same results for the vertical spacers shown in figure 13.

#### 4. Conclusions

In this paper, we demonstrate how a complete design and testing of the micro-mesh detector can be done on a personal computer using a novel BEM algorithm, known as the Robin Hood Solver. We prove that the RH Solver is a reliable and efficient tool for a complete detector design with 300,000

mesh elements, or more, on a single CPU. Owing to the small need for computer resources, we are able to accurately model metal meshes and dielectric objects over an area that is significantly larger than the spatial resolution of the mesh. Our results show that the electron transparency of the mesh is very sensitive to its detailed geometry, while the gain depends only on the bulk properties of the system.

The RH Solver is easily adaptable for a parallel computing environment, or using graphics processors in order to achieve faster calculations for even more detailed geometries [19].

## References

- [1] A. Oed, Nucl. Instrum. Meth. A, **263**, (1988) 351.
- [2] Y. Giomataris, Ph. Rebourgeard, J. P. Robert, and G. Charpak, Nucl. Instrum. Meth. A, **376**, (1996) 29.
- [3] F. Sauli, Nucl. Instr. Meth. A, **386**, (1997) 531.
- [4] See a review of micro-pattern detectors in K. Nakamura et al. (Particle Data Group), J. Phys. G **37**, (2010) 075021.
- [5] <http://garfield.web.cern.ch/garfield/>
- [6] K. Nikolopoulos, P. Bhattacharya, V. Chernyatin, and R. Veenhof, J. Instrum., **6** (2011) P06011.
- [7] P. Lazić, H. Štefančić, and H. Abraham, J. Comput. Phys., **213**, (2006) 117.
- [8] P. Lazić, H. Štefančić, and H. Abraham, Eng. Anal. Bound. Elem., **32**, (2008) 76.
- [9] D. Dujmic et al., Astropart. Phys. **30**, (2008) 58.
- [10] S. F. Biagi, Nucl. Instr. and Meth. A, **421** (1999) 234.
- [11] S. Mukhopadhyay, N. Majumdar, and S. Bhattacharya, J. Instrum., **4**, (2009) P11004.
- [12] <http://www.ansoft.com/products/em/maxwell/>
- [13] <http://www.comsol.com/>
- [14] R. Veenhof, J. Instrum., **4**, (2009) P12017.
- [15] N. Majumdar, and S. Mukhopadhyay, J. Instrum., **2**, (2007) P09006.
- [16] <http://www.artcalc.com/>
- [17] P. Bhattacharya, S. Mukhopadhyay, N. Majumdar, and S. Bhattacharya, Nucl. Instrum. Meth. A, **628**, (2011) 465.
- [18] L. Malter, Phys. Rev. **50**, (1936) 48.
- [19] J. A. Formaggio et al., in preparation.

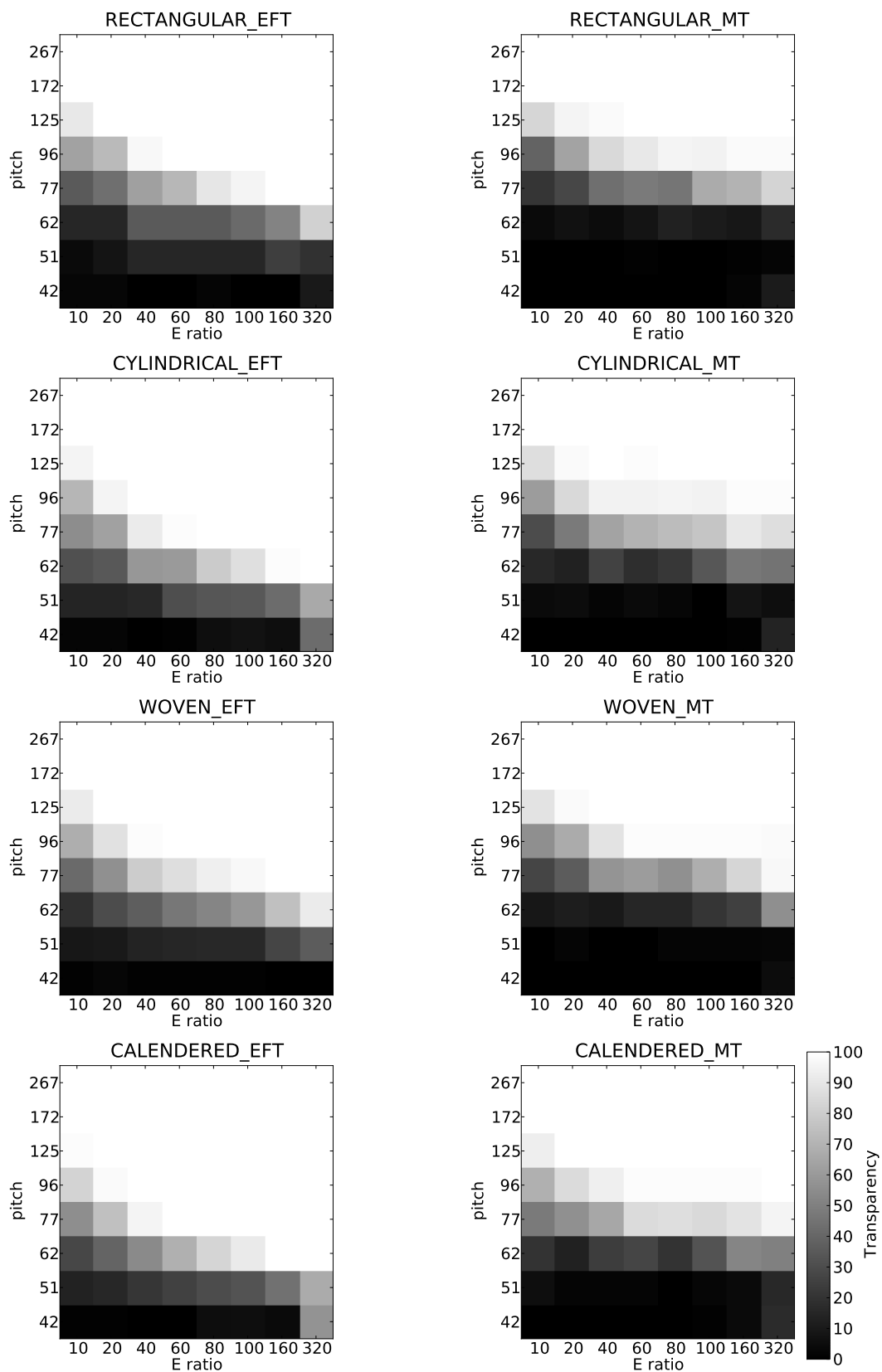


**Figure 4.** Electrical transparencies calculated with EFT and MT methods for different types of meshes. Pitch is given in  $\mu\text{m}$  and with a wire diameter of  $d=28.2 \mu\text{m}$  the pitches and corresponding optical transparencies in percent are 42 (10%), 51 (20%), 62 (30%), 77 (40%), 96 (50%), 125 (60%), 172 (70%) and 267 (80%).

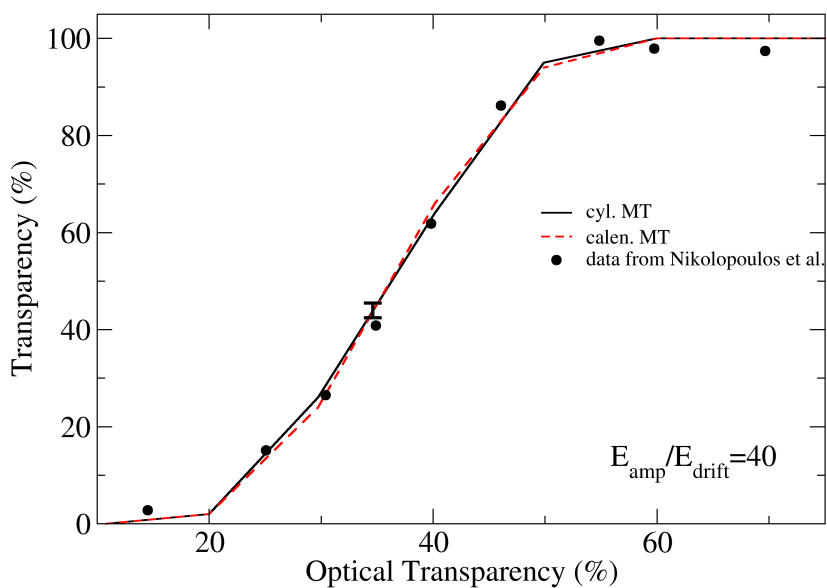


**Figure 5.** The electrical transparency as a function of the optical transparency at the amplification to drift field ratio of 41.4 for cylindrical meshes (solid line) and calendered meshes (dashed line). The dots represent calculated values extracted from the reference [6]. Our mesh is of the same geometry as in the referenced paper (cylindrical). The statistical error for our Monte Carlo simulations of electrical transparency is shown for comparison.

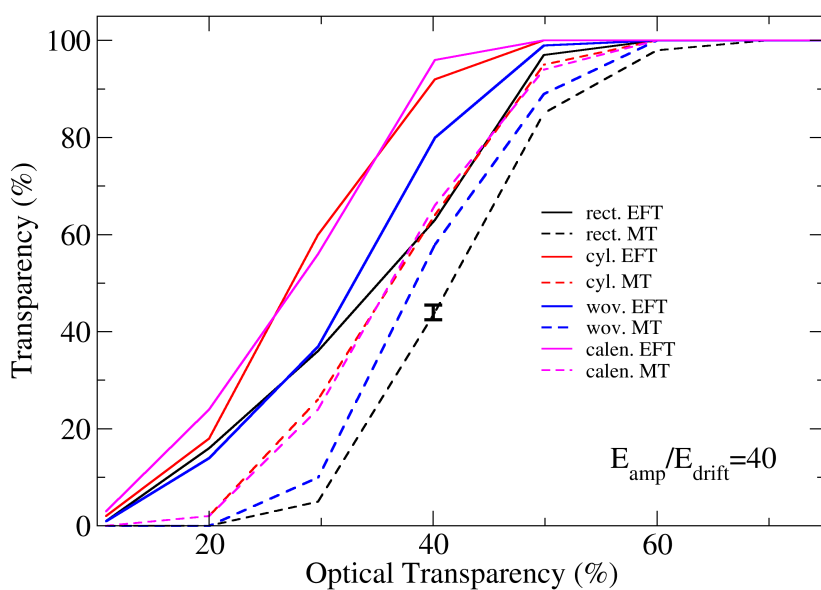


**Figure 6.** Electrical vs. optical transparency. For relation between mesh pitch and optical transparency see caption of figure 4. Full lines show calculation with EFT method while dashed lines represent results of MT calculations. In all cases amplification to drift field ratio is 40. We show the error bar coming from the statistical nature of the Monte Carlo simulations.

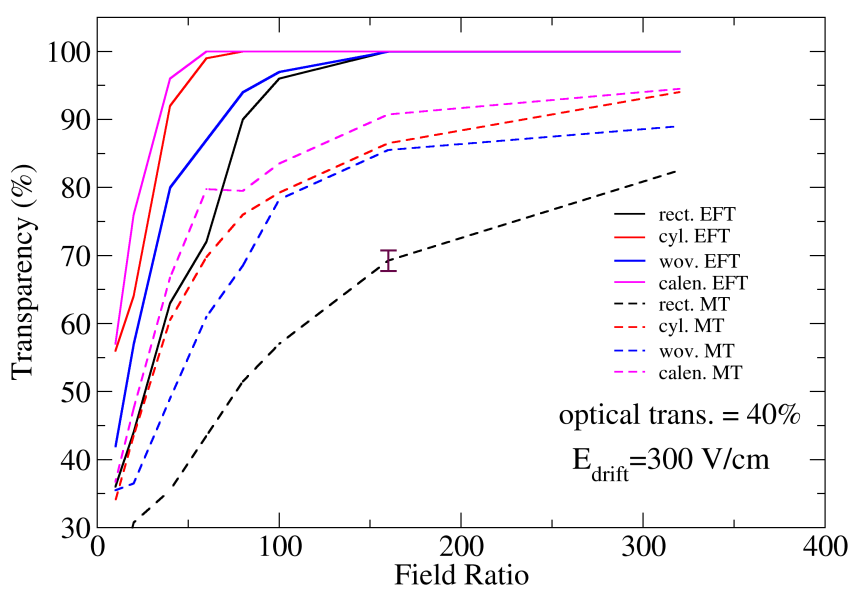


**Figure 7.** Electrical transparency as a function of an amplification to drift field ratio. All four meshes have identical pitch of  $77 \mu\text{m}$  which is equivalent to 40% optical transparency. The error bar is given.

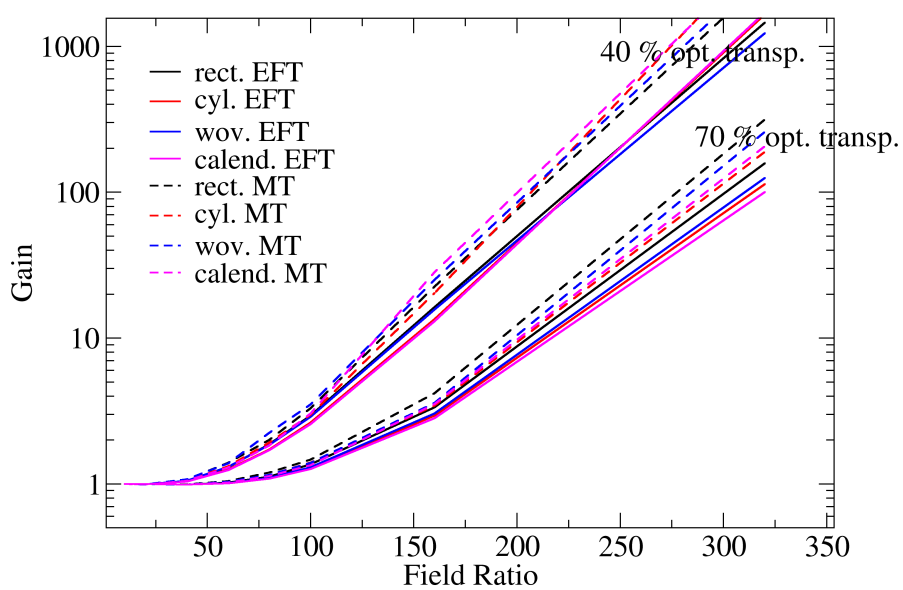


**Figure 8.** Gain as a function of an amplification to drift field ratio for two optical transparencies for all four types of meshes.

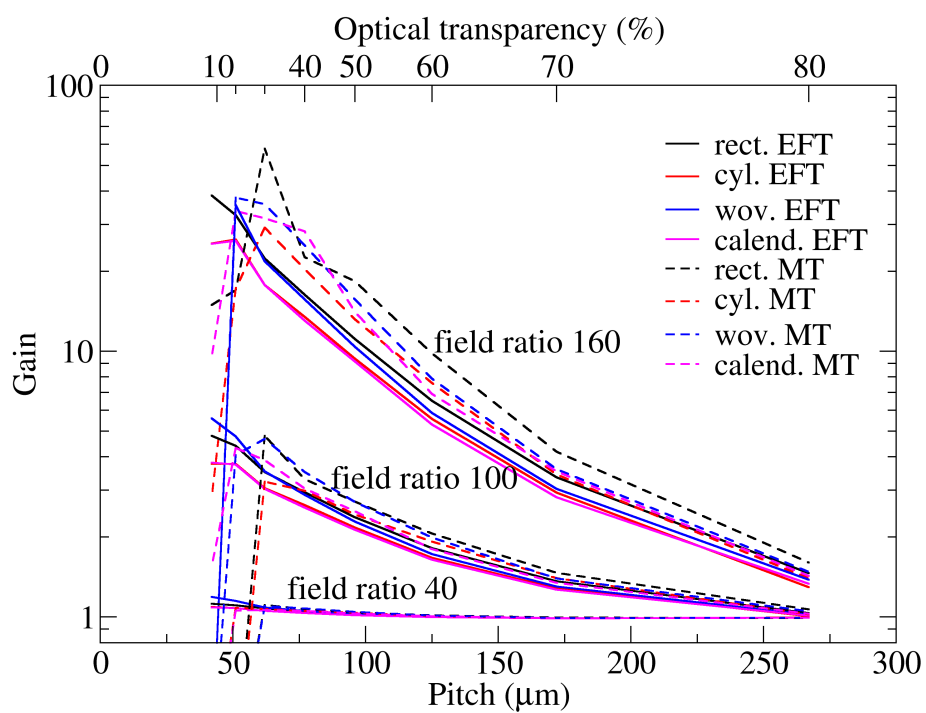


**Figure 9.** Gain as a function of optical transparency for 3 values of amplification to drift field ratio for all four types of meshes.

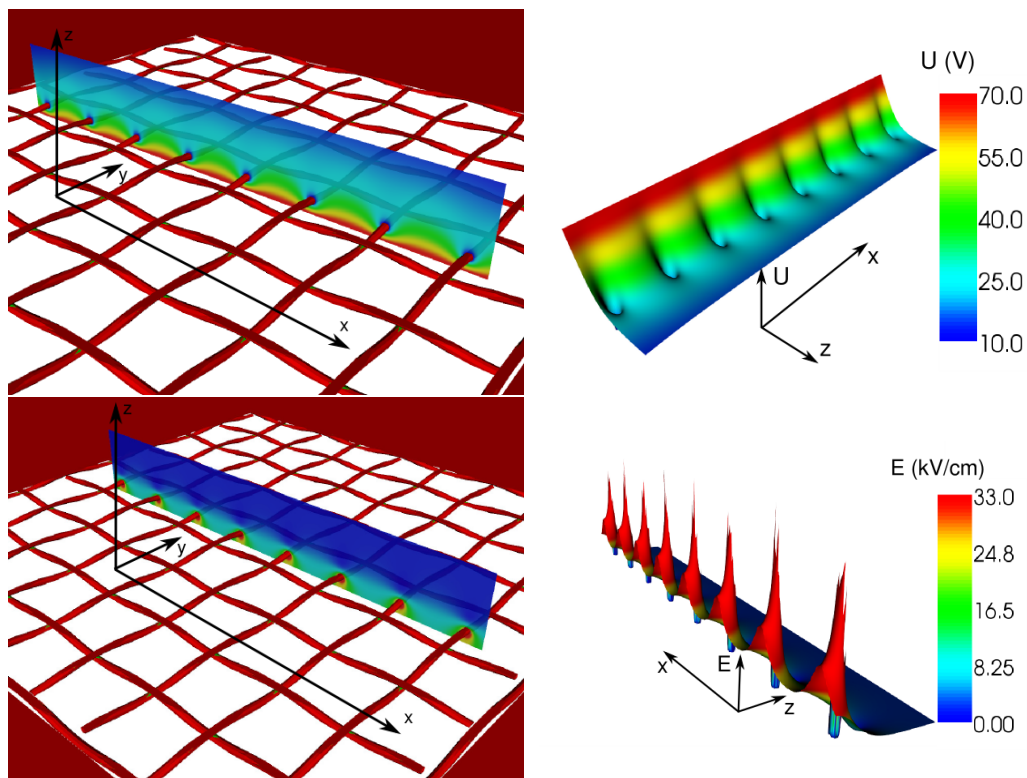


**Figure 10.** Top row: Electric potential shown in a cross section plane - shown on left. Right - the same cross section plane with potential value protruded in the direction perpendicular to the plane. Bottom row: Electric field shown in a cross section plane - shown on left. Right - the cross section plane protruded in perpendicular direction proportionally to the field value. Notice that inside the wire (mesh) electric field drops exactly to zero as expected from the Faraday cage effect.

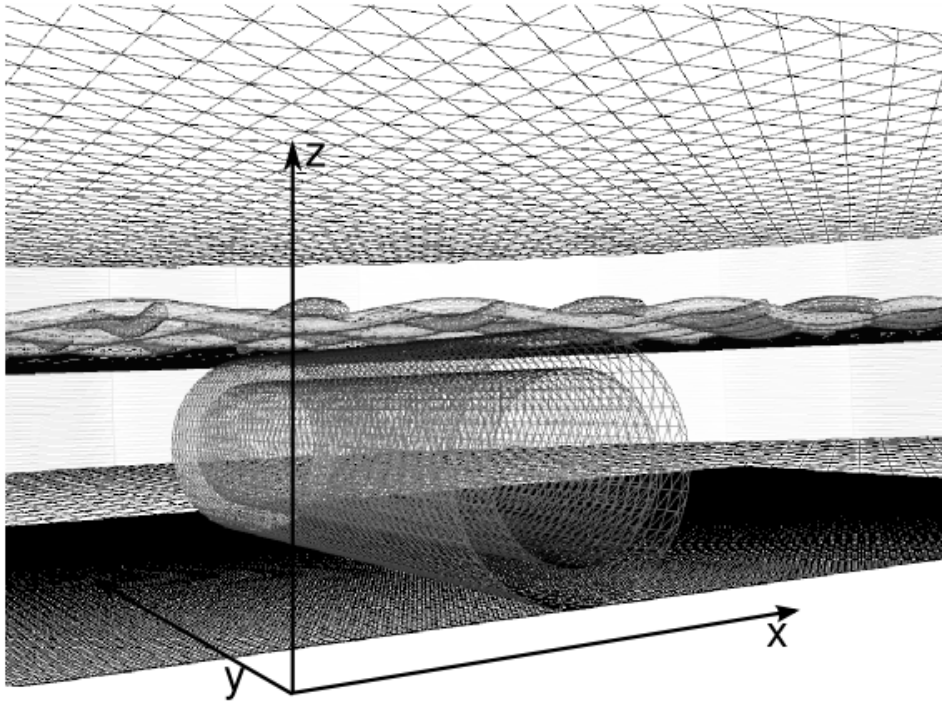


**Figure 11.** Geometry of the dielectric spacer placed between bottom electrode and the mesh. In this figure hollow spacer geometry is shown. Outer diameter of the spacer is  $450 \mu\text{m}$  while inner diameter is  $320 \mu\text{m}$ .

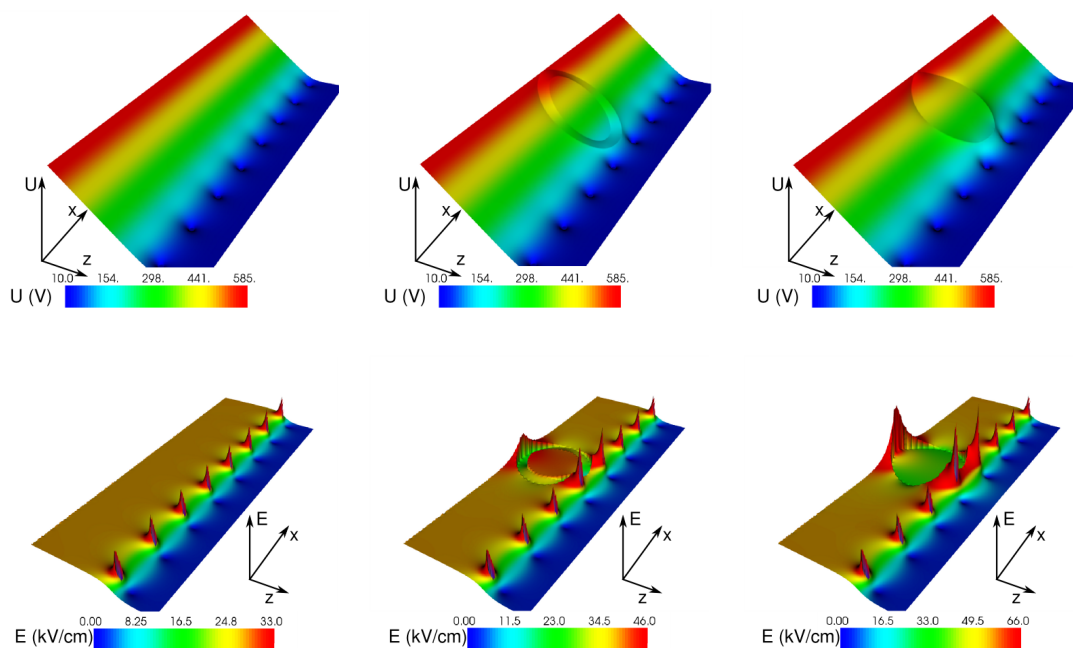


**Figure 12.** Electric potential (top) and field (bottom) along the plane cut shown in figure 10. Left - without spacer. Middle - with hollow (capillary) spacer. Right - with full cylindrical spacer. Comparing maximum electric field values for all three cases gives larger maximum fields for the cases with spacer present. Namely, in the case with hollow spacer maximum field is 1.4 times larger than in the case without a spacer while in the case with the full spacer this factor is 2.0.

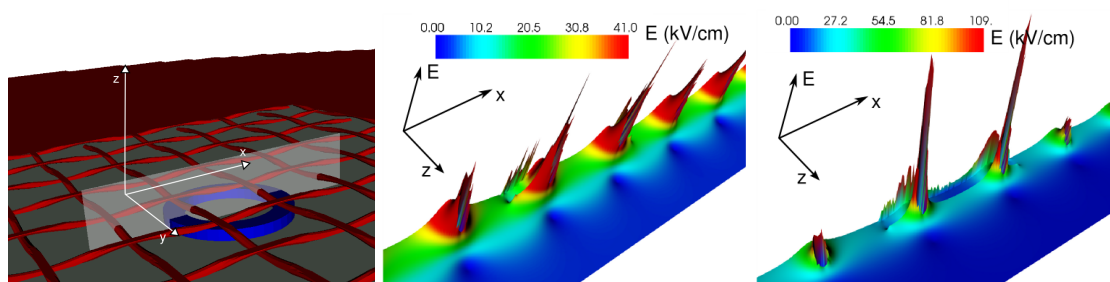


**Figure 13.** Left - geometry of the vertical hollow spacer with the cross section plane in which the electric field is given on the other two images. Middle - electric field in the vertical cross section in a system with hollow spacer. Right - electric field in the vertical cross section in a system with full spacer. Inner and outer diameter of the spacer are  $320 \mu\text{m}$  and  $450 \mu\text{m}$  respectively. The height of the spacer is  $37.8 \mu\text{m}$ . A dielectric spacer causes increase of the electric field compared to a case without a spacer. Moreover, in the case of hollow spacer maximum field value is increased by factor 1.25 while in the case of full spacer maximum field is 3.3 times larger than in the case without the spacer.

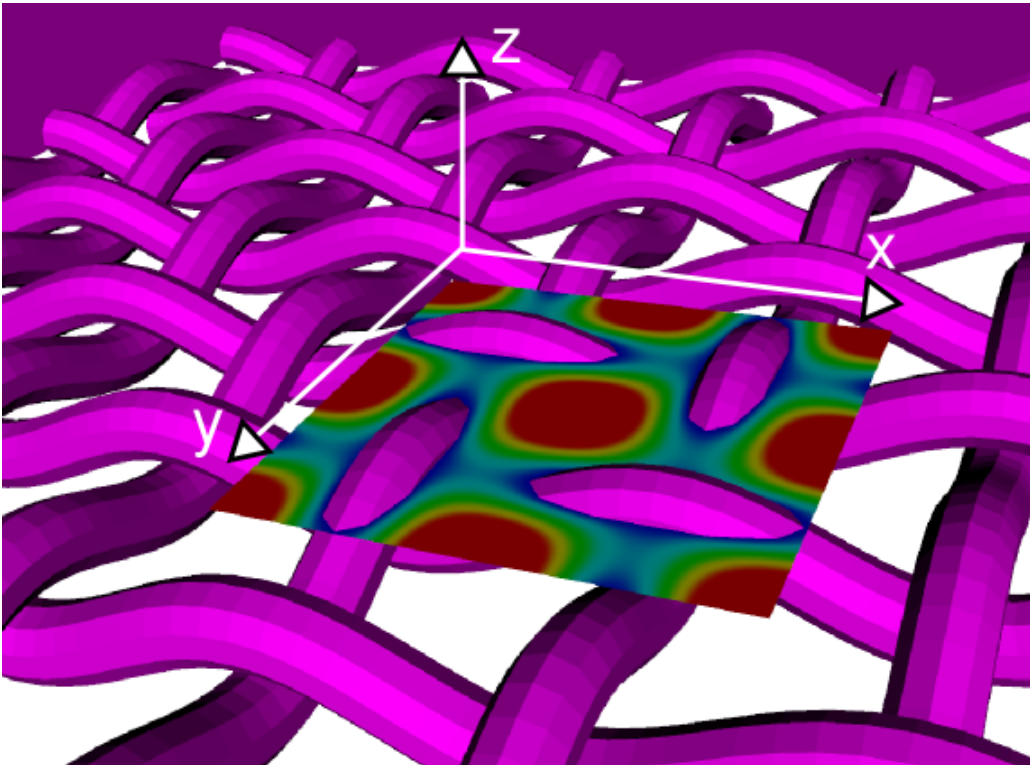


**Figure 14.** Cross section region in a horizontal plane around one hole in the mesh. Detailed electric field values and potentials are shown in figure 15.

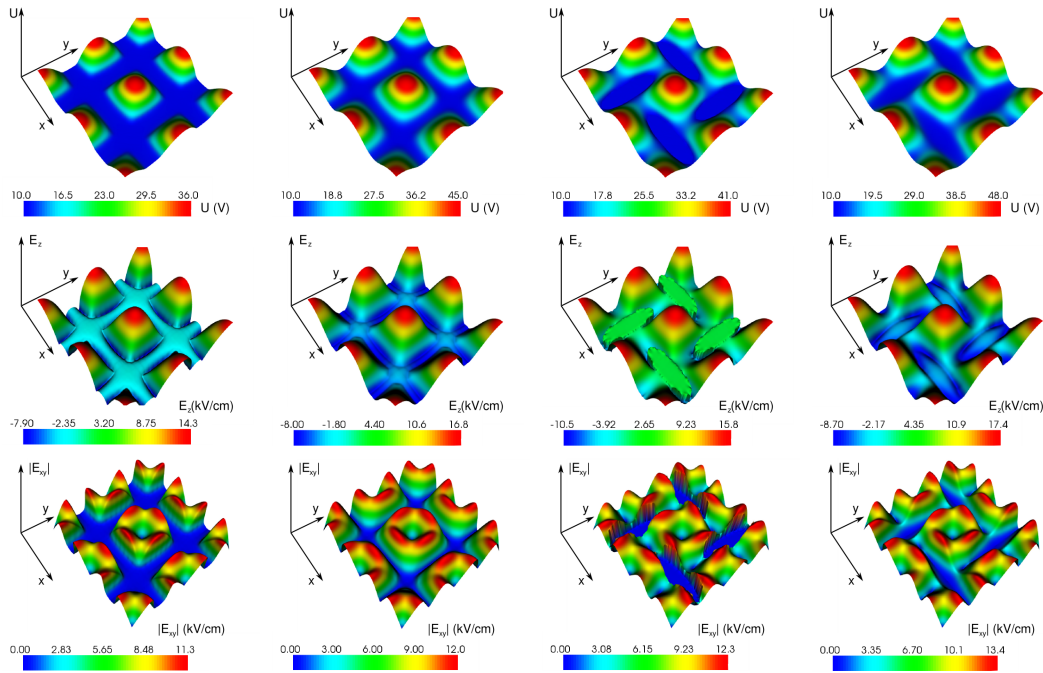


**Figure 15.** Electric potential and field values shown in the plane cut from figure 14. From left to right - rectangular, cylindrical, woven and calendered mesh. From top to bottom - electric potential, vertical ( $E_z$ ) and horizontal ( $E_{xy}$ ) electric field values. All cases are for the mesh pitch of  $96 \mu\text{m}$  and amplification to drift field ratio of 320. Maximal electric field values are shown by red color and in the case of the rectangular mesh component  $E_{xy}$  has the lowest value among all 4 geometries. Scaling it so that rectangular maximum value of the  $E_{xy}$  component is equal to 1, the other geometries have the following maximal values - cylindrical 1.06, woven 1.09, and calendered mesh 1.19, which agrees with our simple explanation of symmetry caused  $E_{xy}$  component cancellation. Even though cylindrical mesh might seem equally symmetrical as the rectangular one the difference is that because of the curvature of the cylindrical wires one gets more of the deflection  $E_{xy}$  component directly above the wire which is not the case for the rectangular mesh in which the surface of the wire is not curved - i.e. is flat. Maximum  $E_z$  component values are again scaled to the rectangular mesh value of 1.0 - cylindrical 1.18, woven 1.10, and calendered mesh 1.21.